JOMAE, In Review
1988

NUMERICAL MODELING OF RATE PROCESSES DURING ICE-STRUCTURE INTERACTION

S. Shyam Sunder, Associate Professor
M.S. Wu, Research Assistant
C.W. Chen, Research Assistant

Massachusetts Institute of Technology, Department of Civil Engineering, Room 1-274, Cambridge, MA 02139

ABSTRACT

The mechanics of the indentation of ice at low to moderate rates of loading is studied using the finite element method. The material model used for the simulation study consists of a multiaxial flow model and a smeared cracking model. The flow model is developed in the formalism of irreversible thermodynamics and, in particular, includes transient creep as an internal rheological variable. A multiaxial criterion is used in the smeared cracking model to predict tensile failure. To solve the initial boundary-value problem, a two-level iterative algorithm is developed. This uses an incremental-iterative method to solve the discretized finite element equations, and a Newton-Raphson technique to solve the constitutive equations of the material model. The objective of the investigation is to study (i) the effects of cracking and transient creep on the ice response, and (ii) the failure modes experienced by the ice sheet during indentation. The influence of velocity and indenter size on the global and maximum local pressures are also investigated. The accuracy of the solutions is examined by varying the time increment and the mesh size used in the analysis.

INTRODUCTION

The prediction of ice forces on fixed offshore structures is one of the classic problems in the study of ice indentation and impact. Recent studies have shown that the magnitude of ice forces is influenced by many parameters including (i) the environmental and loading conditions, e.g., temperature, rate of loading, and type of confinement, (ii) the structural state, e.g., the material integrity and the degree of textural anisotropy, and (iii) the size and shape of the indenter, the aspect ratio, and the type of contact between ice and indenter. Depending on some of these parameters ice can display very complex behavior including elasticity, delayed elasticity, viscous creep, distributed cracking or damage, and tensile cracking. Field observations and small-scale experimental investigations have shown that ice can fail by crushing, spalling, radial and circumferential cracking, buckling, and by a combination of these modes (see,

e.g., the deformation-mode map of Timco [1]).

It has been recognized that the empirical equation given by Korzhavin for predicting ice forces is limited and requires the use of many factors to account for some of the parameters mentioned previously. Understanding of the effects of these parameters on ice forces requires more elaborate theoretical approaches, e.g., the approximate and the finite element methods of analysis. The former method has been used by (i) Michel and Toussaint [2], and Croasdale et al. [3] based on the upper- and lower-bound plasticity solutions, (ii) Ponter et al. [4] based on the reference-stress, power-law creep solution, and (iii) Bruen et al. [5], and Ting and Shyam Sunder [6] based on the upper-bound, power-law creep solutions. The finite element method of analysis has been reported by Shyam Sunder et al. [7], Chehayeb et al. [8] and Tomin et al. [9].

At low strain-rates (e.g. $< 10^{-6}$ s^{-1}) creep flow is the dominant mechanism of deformation. Fracture processes, however, are present during ice-structure interaction, particularly at moderate to high strain-rates (10^{-6} s^{-1} to 10^{-2} s^{-1}). Indentation under these conditions is dominated by progressive fracture or damage which may significantly affect the ice response, especially the local ice pressure acting on the indenter. Furthermore, Palmer et al. [10] and Cormeau et al. [11] have shown that at high rates of loading ($> 10^{-2}$ s^{-1}) brittle fracture models can predict global indentation pressures several orders of magnitude less than those predicted by elastic-plastic or crushing models.

The strains produced in ice during interaction with an indenter can be very small. For example, it has been reported that a surface maximum strain of 0.15% was measured in a floating platform toward the end of a drilling season of three months (see Sinha et al. [12]). Laboratory tests by Cox et al. [13] on multi-year sea ice have shown that the failure strain at peak uniaxial compressive stress falls within the range of 0.05% and 0.20%. This is consistent with the test results of Frederking and Timco [14], and Sinha [15] for sea ice, as well as those of Sinha [16] for freshwater ice. Triaxial confinement in a compression test increases the failure strain, but this is usually no more than 1%-2% (Jones [17]; Cox et al. [13]). As noted by Sinha et al. [12], for problems involving brittle failure (such as high loading rate and bending) steady-state creep is not reached and the fracture strains are approximately 0.05%. Over this range of deformation transient creep (anelsticity) rather than steady-state creep is the dominant mechanism of flow.

The above discussion points to the inadequacy of the use of an elastic-power

law or elastic-plastic model in ice-structure interaction problems involving moderate and high loading rates where crushing and brittle fracture may occur before steady state is reached. Deformations associated with transient creep and cracking, as opposed to steady-state creep, are thus major considerations in a great variety of applied ice mechanics problems.

The objective of this paper is to numerically study the rate processes of ice indentation at low to moderate rates of loading. For this purpose an infinite ice sheet loading a vertical rigid cylinder under plane stress conditions and at the temperature of -10°C is considered. Attention is focussed on the effect of cracking on the indentation pressures, the propagation of cracks through the ice sheet, and the effect of transient deformation on the ice response. The influence of velocity, indenter size, time increment and mesh size on the numerical results serve as test cases for the simulations.

The finite element method of analysis is used in the numerical study in conjunction with a multiaxial differential flow model (Shyam Sunder and Wu [18, 19]) and the smeared cracking model (Rashid [20]). The flow model is developed in the formalism of irreversible thermodynamics with internal state variables and can model elasticity, transient creep as well as steady-state creep. The smeared crack, which refers to a band of uniformly and continuously distributed microcracks, is widely used in the finite element analysis of concrete and rock fracture. A multiaxial strength criterion is used to predict tensile failure in the model.

The coupled, nonlinear and time-dependent constitutive equations of the model are stiff and pose severe constraints on the development of a finite element solution. To solve the constitutive equations, a Newton-Raphson iteration technique combined with the α-method of time integration is used to accelerate convergence. The discretized system of finite element equations, on the other hand, are solved with an incremental-iterative method in which the incremental tangent stiffness matrix is updated at each iteration using the BFGS technique.

MULTIAXIAL DIFFERENTIAL MODEL

A constitutive model of flow in orthotropic polycrystalline ice has been developed by Shyam Sunder and Wu [19]. Since only small deformations are considered, the total strain is additively decomposed into the steady-state, transient and elastic components. Two groups of state variables are identified: the observable and the internal variables. The dissipation associated with

isotropic hardening is described by a scalar internal variable p, while the dissipative mechanisms of steady-state and transient flow are described by the tensorial internal rheological variables $\underline{\varepsilon}_v$ and $\underline{\varepsilon}_t$, respectively. The total strain tensor $\underline{\varepsilon}$ is taken to be the observable state variable. The instantaneous elastic deformation $\underline{\varepsilon}_t$ and the time-dependent anelastic deformation are described by linear elasticity theory. Since transient deformation in polycrystalline ice is recoverable it is taken to represent the anelastic deformation. The anelastic deformation tensor is linearly proportional to the back-stress tensor $\underline{R}$ generated during kinematic hardening.

The constitutive equations are derived from the Helmholtz free energy and the dissipation potentials. Restrictions imposed by the Clausius-Duhem inequality on the free energy yields the equations-of-state which relate the state variables ($\underline{\varepsilon}$, $\underline{\varepsilon}_v$, $\underline{\varepsilon}_t$, p) to their respective thermodynamic forces ($\underline{\sigma}$, $\underline{\sigma}$, $\underline{\sigma}_d$, -BV), where $\underline{\sigma}$ is the stress tensor, $\underline{\sigma}_d = \underline{\sigma} - \underline{R}$ is the reduced stress tensor, and BV is a scalar drag-stress measure. The variable B represents a non-dimensional drag-stress, while V is a temperature-dependent stress-factor given by $V=V_o \exp(Q/NRT)$, in which the constants V_o, Q, N, R and T denote a temperature-independent constant, the activation energy for steady-state (and transient) creep, the power law constant, the universal gas constant and the temperature in Kelvin, respectively. The evolution equations for the internal variables are obtained by normality of the thermodynamic fluxes (time rates of change of the internal variables) to the dissipation potential expressed in terms of the thermodynamic forces. These equations are specialized for an isotropic material and summarized below in engineering matrix notation.

(a) Strain-Rate Decomposition

$$\dot{\underline{\varepsilon}} = \dot{\underline{\varepsilon}}_e + \dot{\underline{\varepsilon}}_t + \dot{\underline{\varepsilon}}_v \tag{1}$$

(b) Equations-of-State

$$\dot{\underline{\sigma}} = \underline{D}\dot{\underline{\varepsilon}}_e = \underline{D}(\dot{\underline{\varepsilon}} - \dot{\underline{\varepsilon}}_t - \dot{\underline{\varepsilon}}_v) \tag{2}$$

$$\underline{\varepsilon}_d = \underline{\sigma} - \underline{R} \tag{3}$$

$$\underline{R} = 2/3\ AE\ \underline{H}\ \underline{\varepsilon}_t \quad \text{or} \quad \underline{S}_R^{\,*} = \underline{G}\ \underline{R} = (2/3)\ AE\ \underline{\varepsilon}_t \tag{4}$$

where $\underline{D}$ denotes the classical elastic rigidity matrix, and $\underline{H}$, $\underline{G}$ denote the strain-rate and stress transformation matrices, respectively. The latter

two matrices are linear operators transforming strain-rate and stress vectors into deviatoric components. They are given by:

$$\underline{H} = \begin{bmatrix} 2/3 & -1/3 & -1/3 & & & \\ & 2/3 & -1/3 & & & \\ & & 2/3 & & & \\ & & & 1/2 & & \\ \text{Symmetric} & & & & 1/2 & \\ & & & & & 1/2 \end{bmatrix} \tag{5a}$$

and

$$\underline{G} = \begin{bmatrix} 2/3 & -1/3 & -1/3 & & & \\ & 2/3 & -1/3 & & & \\ & & 2/3 & & & \\ & & & 2 & & \\ \text{Symmetric} & & & & 2 & \\ & & & & & 2 \end{bmatrix} \tag{5b}$$

Also, the rigidity matrix contains two parameters E and ν which denote Young's modulus and Poisson's ratio, respectively. The parameter AE represents an anelastic modulus of kinematic hardening. Since transient deformation is considered to be incompressible, the relevant Poisson's ratio has the value of 0.5. For the temperature range of -5°C to -40°C, the parameters ν, E and AE can be taken to be temperature-independent constants.

(c) Evolution Equations

$$\underline{\dot{\varepsilon}}_v / \dot{\varepsilon}_o = \lambda \, \underline{S}^* = \lambda \, \underline{G} \, \underline{\sigma} \tag{6}$$

$$\underline{\dot{\varepsilon}}_t / \dot{\varepsilon}_o = \lambda_d \underline{S}_d^* = \lambda_d \, (\underline{S}^* - \underline{S}_R^*) \tag{7}$$

$$\dot{B} = (\tilde{H} E / \sigma_{d,eq}) \, \dot{\varepsilon}_{t,eq} \tag{8}$$

In Eqs. (6) - (8), $\dot{\varepsilon}_o$ is a reference strain-rate of unity, and $\tilde{H}$ is a temperature-independent constant. The superposed dot denotes time derivative while the subscript 'eq' denotes equivalent value. The initial value of BV is denoted by $B_o V$. The evolution equation for the steady-state strain as given by Eq. (6) is the classical power law formulation where the principal axes of the steady-state strain-rate and the deviatoric stress coincide. The parameter λ is a function of the equivalent stress

$$\sigma_{eq}^2 = 3/2 \, \underline{\sigma}^T \underline{G} \, \underline{\sigma} = 3/2 \, \underline{S}^{T*} \underline{H} \, \underline{S}^* \tag{9a}$$

and has the following explicit form:

$$\lambda = 3/2\ (1/V)^N\ \sigma_{eq}^{N-1} \tag{9b}$$

If $\underline{\sigma}$ and V in Eq. (6) are replaced by $\underline{\sigma}_d$ and BV respectively, the evolution equation for the transient strain (Eq. (7)) is obtained. The parameter λ_d is a function of the equivalent reduced stress

$$\sigma_{d,eq}^{\ 2} = 3/2\ \underline{\sigma}_d^{\ T} \underline{G}\ \underline{\sigma}_d = 3/2\ \underline{S}_d^{\ T*} \underline{H}\ \underline{S}_d^{\ *} \tag{9c}$$

and has a form similar to Eq. (9b):

$$\lambda_d = 3/2\ (1/BV)^N\ \sigma_{d,eq}^{\ N-1} \tag{9d}$$

Finally, the equivalent transient strain-rate that appears in Eq. (8) can be determined from the strain-rate transformation matrix, i.e.:

$$\dot{\varepsilon}_{t,eq}^{\ 2} = 2/3\ \dot{\underline{\varepsilon}}_t^{\ T} \underline{H}\ \dot{\underline{\varepsilon}}_t \tag{9e}$$

The values of the model parameters E, υ, N, V, A, B_o, $\tilde{H}$ and the variables Q, R, T used in the numerical simulations are listed in Table 1.

TENSILE CRACK MODEL

Smeared Cracking Model.-- The discrete and smeared cracking models are the two methods of crack representation commonly used in the finite element analysis of fracture in rock and concrete. However, the discrete crack representation has the disadvantages of a non-automatic method of defining the inter-element line cracks and a lack of generality in modeling their directions (Bazant and Cedolin [21]). The smeared cracking concept, which models fracture as bands of cracks smeared through the entire finite element, does not suffer from these shortcomings and is consequently used in this study.

The indentation process is simulated under plane stress conditions, i.e., the thickness of the ice sheet is small compared to the diameter of the cylindrical indenter. It is further assumed that no cracks exist in the ice sheet prior to indentation. A crack is assumed to form when the stresses satisfy a tensile failure criterion. The orientation of the crack is orthogonal to the direction of

the principal tensile stress, except when the stress field is purely compressive, in which case the the normal of the crack is assumed to lie in the direction of the smallest compressive stress. Once the crack is formed, the material is incapable of carrying stress in the direction normal to the crack face. The originally isotropic stiffness matrix is changed into an orthotropic one, i.e., the modulus in the direction of the crack normal is reduced to zero. No shear retention is allowed, and the Poisson effect is neglected. However, the material parallel to the crack is still capable of carrying stress and a secondary crack orthogonal to the first one may form subsequently. The stiffness of the material is completely lost only when both orthogonal systems of cracks are formed.

Tensile Failure Criterion.-- A rate-sensitive multiaxial failure criterion appropriate for ice, proposed by Ting and Shyam Sunder [22], is adopted in this study. This criterion recognizes that (i) at loading rates smaller than a certain threshold strain-rate, which for a grain size of 5mm and at -10°C is approximately 5×10^{-8} s^{-1} in uniaxial tension and approximately 10^{-6} s^{-1} in uniaxial compression, rate-dependent flow is the dominant mechanism of deformation, (ii) at loading rates greater than the ductile to brittle transition strain-rate (e.g. 10^{-2} s^{-1}) brittle fracture dominates in either tension and compression, and (iii) at intermediate loading rates fracture becomes increasingly important relative to flow as the strain-rate increases from the threshold to the high strain-rate.

The multiaxial criterion must be capable of describing the failure conditions under uniaxial loadings. In uniaxial tension, the stress to nucleate a crack is in general the fracture stress (tensile strength) σ_{tf}. This is modeled by the following equation:

$$1/\sigma_{tf} = 1/\sigma_{tm} + 1/[W\ (\dot{\varepsilon}/\dot{\varepsilon}_o)^{1/N}] \qquad (10)$$

where σ_{tm} denotes the limiting fracture strength at the ductile to brttle transiton strain-rate. The parameter W is the counterpart of the parameter V in the flow model and follows the Arrhenius law. In uniaxial compression, the stress at which the first crack nucleates is defined to be the "yield" stress. This is postulated to occur when the lateral tensile strain equals the fracture strain predicted by Eq. (10) under constant strain-rate tests. Once the yield stress is reached, the material continues to sustain compressive load but loses its ability to carry tensile load in the transverse direction. The compressive yield strength σ_{cn} is described by the following equation:

$$1/\sigma_{cn}^{\ 2} = 1/\sigma_{cm}^{\ 2} + 1/[V\ (\dot{\varepsilon}/\dot{\varepsilon}_o)^{1/N}]^2 \qquad (11$$

where σ_{cm} denotes the limiting fracture strength at the ductile to brittle transition strain-rate. Eqs. (10) and (11) state that the tensile strength and the compressive yield strength increase with strain-rate, but become insensitive to this parameter at high rates of loading.

To generalize the above formulation to three dimensions, a rate-sensitive and isotropic Drucker-Prager failure surface is proposed. This failure surface is expressed as follows:

$$f(\underline{\sigma}) = pI_1 + J_2^{\ 1/2} - k \qquad (12)$$

where $I_1 = \sigma_{xx} + \sigma_{yy} + \sigma_{zz}$ is the first invariant of stresses and $J_2 = 1/2\ \underline{\sigma}^T \underline{G}\ \underline{\sigma}$ is the second invariant of the deviatoric stresses. Failure occurs when $f(\underline{\sigma}) = 0$. The constants p and k at a given equivalent strain rate can be derived from two uniaxial tests at the same constant strain-rate value, one in tension and the other in compression. The resulting equations are:

$$p = \frac{1}{3^{1/2}}\ \frac{(-\sigma_{cn}/\sigma_{tf}) + 1}{(-\sigma_{cn}/\sigma_{tf}) - 1} \qquad (13)$$

and

$$k = -\sigma_{cn}(p - 1/3^{1/2}) = \sigma_{tf}(p + 1/3^{1/2}) \qquad (14)$$

where the numerical value for the compressive stress σ_{cn} is taken to be positive. Since σ_{cn} and σ_{tf} are given by Eqs. (10) and (11), p and k are dependent on strain-rate. For strain-rates below the threshold value in tension, i.e., approximately $5 \times 10^{-8}\ s^{-1}$, pressure-insensitive flow dominates and $\sigma_{cn} = \sigma_{tf}$. This implies that $p = 0$ and k is proportional to the equivalent stress, and the failure surface reduces to the von Mises flow surface. At high strain-rates, e.g., above $10^{-2}\ s^{-1}$, no flow can occur and elastic deformation is followed by brittle fracture. The failure surface is strictly a fracture surface. At intermediate strain-rates, the failure surface becomes a yield/fracture surface, i.e., a crack forms as long as the criterion is satisfied, but in the case of a purely compressive state of stress, the crack will nucleate in a plane perpendicalar to

the direction of the smallest compressive stress and will remain stable, although it cannot support any tensile stress that subsequently might act across its surface.

A quadrilateral isoparametric element is used for the current numerical analysis. Stresses are evaluated at the four Gaussian points and an element is considered to be completely fractured only when the failure criterion is satisfied at the two orthogonal directions at all four Gaussian points.

The strength criterion has been shown by Bazant and Cedolin [21] to yield unobjective solutions, i.e., the numerical results depend on the size of the mesh used in the finite element analysis. This is generally found to be true for the strain softening portion of the predicted stress-strain curve, although some results have indicated that the peak stress may not be affected. Consequently, it is necessary to investigate the discrepancies, if any, between the solutions obtained from different mesh sizes. The strength criterion rather than an objective energy criterion based on fracture mechanics is used in the current study because of the relative ease of implementation of the former in solving problems involving hundreds of cracks.

The values of the fracture model parameters σ_{cm}, σ_{tf} and W used in the current study are listed in Table 1.

FINITE ELEMENT FORMULATION

An important factor in the development of finite element analysis is the proper selection of a solution algorithm. Nonlinear problems, in general, require the solution of a set of coupled, nonlinear algebraic equations. In addition, the problems may be path-dependent (e.g., plasticity, non-conservative loading) or they may possess multiple solutions (e.g., snap-through buckling). Also, considerable difficulty may be encountered when the time-dependent constitutive equations of the material model are stiff (Cordts and Kollman [23]).

In the current model, the discretized system of nonlinear equations are solved with an incremental-iterative method. A number of iterations are performed during each load step to dissipate residual forces until a convergence criterion is satisfied. Two alternative criteria are used, one based on the norm of the increment in the displacement vector, and the other on the increment in internal energy. The tangent stiffness matrix is updated at each iteration using the BFGS quasi-Newton method (Matthies and Strang [24]). This combines the advantages of rapid convergence of the full Newton-Raphson method, in which full reformation of

the stiffness matrix is performed at each iteration, and the economy of the modified Newton-Raphson method, in which stiffness matrix update is only carried out on an accepted equilibrium configuration.

A nonlinear equation solver is used in conjunction with a numerical time integrator to solve the constitutive equations for the incremental stresses and incremental creep (transient and steady-state) strains. For rapid convergence, use is made of the Newton-Raphson or tangent type iteration and the α-method of numerical time integration (Chehayeb et al. [8]).

Solution of Finite Element Equations.-- In rate problems it is convenient to formulate the finite element equations in incremental form. The basic approach in an incremental technique is to assume that the solution at time t_i is known, and that the solution at time t_{i+1} is required. The discretized system of equations at time t_{i+1} can be written as:

$$\underline{R}_{i+1}^{\,j} = \underline{P}_{i+1} - \underline{F}_{i+1}^{\,j} \tag{15}$$

where $\underline{P}$, $\underline{F}=\underline{F}(\underline{U})$ and $\underline{R}=\underline{R}(\underline{U})$ represent the vectors of the nodal external, internal, and residual forces, respectively, and $\underline{U}$ is the nodal displacement vector. The superscript j denotes the iteration number within a given time step. Note that the external force vector is assumed to be independent of the displacement. In the incremental-iterative method, the incremental nodal displacement and residual force vectors are defined respectively as follows:

$$\underline{d}_{i+1}^{\,j} = \underline{U}_{i+1}^{\,j+1} - \underline{U}_{i+1}^{\,j} \tag{16}$$

$$\underline{r}_{i+1}^{\,j} = \underline{R}_{i+1}^{\,j} - \underline{R}_{i+1}^{\,j+1} \tag{17}$$

The incremental displacements and residual forces are related by the incremental stiffness matrix $\underline{K}$, i.e.:

$$\underline{K}_{i+1}^{\,j}\ \underline{d}_{i+1}^{\,j} = \underline{r}_{i+1}^{\,j} \tag{18}$$

Eq. (18) is the so-called Quasi-Newton equation. The internal force vector is defined as:

$$\underline{F}_{i+1}^{\,j} = \int \underline{B}^{T}\ \underline{\sigma}_{i+1}^{\,j}\ d\Omega \tag{19}$$

where Ω is the volume of the element, and $\underline{B}$ is the incremental (in the sense of an increment from time t_i to t_{i+1}) strain-nodal displacement matrix given by:

$$\Delta\underline{\varepsilon} = \underline{B}\Delta\underline{U} \tag{20}$$

The evaluation of the integral in Eq. (19) is based on a Gaussian quadrature formula.

Noting Eq. (20), the constitutive relations expressed by Eqs. (1) and (2) may be rewritten as a set of incremental element stress-nodal displacement relations:

$$\Delta\underline{\sigma} = \underline{DB}\Delta\underline{U} - \underline{D}\Delta\underline{\varepsilon}_{cr} \tag{21}$$

where $\Delta\underline{\varepsilon}_{cr}$ represents $\Delta\underline{\varepsilon}_t + \Delta\underline{\varepsilon}_v$, and $\underline{D}$ is the rigidity matrix. Eq. (21) can be put into the following alternative form:

$$\underline{\sigma}_{i+1} - \underline{\sigma}_i = \underline{DB}(\underline{U}_{i+1} - \underline{U}_i) - \underline{D}(\underline{\varepsilon}_{cr,i+1} - \underline{\varepsilon}_{cr,i}) \tag{22}$$

Creep strains that appear in Eq. (22) are nonlinear functions of stress since λ and λ_d (Eqs. (6) and (7)) are not constants.

A two-level iterative algorithm is used to solve (the global form of) Eqs. (15)-(18) as well as the constitutive relation (Eq. (22)) for $\underline{U}_{i+1}$ at each new time step t_{i+1}. A line search procedure is used in the upper level (BFGS) algorithm to minimize the component of the residual force in some search direction. This procedure "damps" or scales the incremental displacement vector in order to improve convergence characteristics of the iterative algorithm. It requires, in effect, another subset of iterations until a specified tolerance is not exceeded. Details of the BFGS method can be found in Matthies and Strang [24] and Crisfield [25]. An outline of the algorithm is provided below:

(1) For each load increment determine a new incremental displacement vector $\underline{d}'$ using the following equation:

$$\underline{d}'^{\,j}_{i+1} = \underline{K}^{j,-1}_{i+1}\,\underline{R}^{j}_{i+1} \tag{23}$$

This new vector defines the direction for the actual incremental displacement vector $\underline{d}$.

(2) The true displacement increment is determined from the following equation:

$$\underline{d}_{i+1}{}^{j} = \underline{U}_{i+1}{}^{j+1} - \underline{U}_{i+1}{}^{j} = \eta^{j}\underline{d}'_{i+1}{}^{j} \tag{24}$$

where η^j is a step-length multiplier. The line search is initialized with a value of $\eta^j = 1$. With the displacement increment determined from Eq. (24), compute the incremental stress and incremental creep strain vectors from Eq. (22) using the iterative algorithm (lower-level iteration in k) to be described later. In the first iteration on Eq. (22) the incremental creep strain vector is assumed to be a zero vector.

(3) Update the internal force vector using the newly found incremental stress vector and Eq. (19). This yields $\underline{F}_{i+1}{}^{j+1}$. The residual force vector $\underline{R}_{i+1}{}^{j+1}$ can then be computed using Eq. (15). Next, the line search procedure requires the residual force vector $\underline{R}$ and the incremental displacement vector $\underline{d}'$ to satisfy the following inequality:

$$\left| \frac{\underline{d}'_{i+1}{}^{j,T}\ \underline{R}_{i+1}{}^{j+1}}{\underline{d}'_{i+1}{}^{j,T}\ \underline{R}_{i+1}{}^{j}} \right| \leq \zeta \tag{25}$$

where ζ for a slack search is greater than 0, e.g., 0.8. If the tolerance limit is violated, η^j is varied and the calculations in steps (2) and (3) are repeated until Eq. (25) is satisfied. The vectors $\underline{U}_{i+1}{}^{j+1}$, $\underline{R}_{i+1}{}^{j+1}$ corresponding to the final accepted value of η^j determine the incremental values $\underline{d}_{i+1}{}^{j+1}$ and $\underline{r}_{i+1}{}^{j+1}$ in Eqs. (16) and (17). Convergence is checked at this point. If convergence is not yet attained, the incremental values are used to update the inverse stiffness matrix as outlined in step (4).

Two convergence criteria are used: (a) Ratio of norm of displacement increment vector to norm of displacment vector at given time step is $\leq$ 0.001; and (b) absolute value of the ratio of the internal energy at iteration j+1 to the initial internal energy is $\leq$ 0.001, i.e.:

$$\left| \frac{\underline{d}_{i+1}{}^{j+1,T}\ \underline{R}_{i+1}{}^{j+1}}{\underline{d}_{i+1}{}^{0,T}\ \underline{R}_{i+1}{}^{0}} \right| \leq 0.001 \tag{26}$$

Typically, four or five iterations are required for convergence at the higher level if updating of the tangent stiffness by the BFGS method is used. On the other hand, the modified Newon-Raphson method requires ten or more iterations for convergence, and is unstable for high-rate simulations.

(4) The updating of the inverse stiffness matrix is carried out according to the following formula:

$$\underline{K}_{i+1}^{j+1,-1} = (\underline{I} + \underline{v}^{j+1}\underline{w}^{j+1,T})\, \underline{K}_{i+1}^{j,-1}\, (\underline{I} + \underline{w}^{j+1}\underline{v}^{j+1,T}) \tag{27}$$

where $\underline{v}^{j+1}$ and $\underline{w}^{j+1}$ are specially chosen vectors which are functions of $\underline{d}_{i+1}^{j+1}$ and $\underline{r}_{i+1}^{j+1}$ (see, e.g., Matthies and Strang [24]). The updated inverse stiffness matrix is used in step (1) for the next iteration.

Numerical Integration of the Constitutive Equations.--The evaluation of the incremental stresses and incremental creep strains (lower-level iteration) requires the simultaneous consideration of Eqs. (22), (6), and (7). This involves the use of incremental creep strain from iteration k to evaluate the incremental stress for iteration k+1 using Eq. (22). The incremetal creep strain for iteration k+1 is then evaluated with the α-method of numerical integration. For the viscous strain, this requires:

$$\Delta\underline{\varepsilon}_v = \underline{\varepsilon}_{v,i+1} - \underline{\varepsilon}_{v,i} = \dot{\varepsilon}_o \lambda_\alpha \underline{S}_\alpha^* \Delta t \tag{28}$$

where $\underline{S}_\alpha^*$ is a weighted average of the deviatoric stress vector in the time interval $\Delta t = (t_{i+1}-t_i)$ and λ_α is derived from Eq. (9a) by weighting on the stresses, i.e.:

$$\underline{S}_\alpha^* = (1 - \alpha)\underline{S}_i^* + \alpha \underline{S}_{i+1}^* \tag{29}$$

$$\lambda_\alpha = 3/2\ (1/V)^N\ (3/2\ \underline{S}_\alpha^{*T}\underline{H}\ \underline{S}_\alpha^*)^{(N-1)/2} \tag{30}$$

Note that use has been made of Eq. (9b) in arrivng at Eq. (30). The analogous nature of the flow equations for steady-state and transient creep implies that Eqs. (28) - (30) become the appropriate expressions for the transient strain when

$\underline{\varepsilon}_v$, λ_α, and $\underline{S}_\alpha^*$ are replaced by $\underline{\varepsilon}_t$, $\lambda_{d,\alpha}$, and $\underline{S}_{d,\alpha}^*$, respectively, i.e.:

$$\Delta\underline{\varepsilon}_t = \dot{\varepsilon}_o \lambda_{d,\alpha} \underline{S}_{d,\alpha}^* \Delta t = \dot{\varepsilon}_o \lambda_{d,\alpha} (\underline{S}_\alpha^* - \underline{S}_{R,\alpha}^*) \Delta t \tag{31}$$

$$\underline{S}_{d,\alpha}^* = (1 - \alpha)\underline{S}_{d,i}^* + \alpha \underline{S}_{d,i+1}^* \tag{32}$$

$$\lambda_{d,\alpha} = 3/2 \ (1/B_\alpha V)^N \ (3/2 \ \underline{S}_{d,\alpha}^{*T} \underline{H} \ \underline{S}_{d,\alpha}^*)^{(N-1)/2} \tag{33}$$

Note that the expressions for the transient strain require knowledge of the α-value of the variables $\underline{S}_R^*$ and B. In general, it is desirable to solve for all the unknowns (i.e., $\Delta\underline{\sigma}$, $\Delta\underline{R}$, ΔB, $\Delta\underline{\varepsilon}_v$, $\Delta\underline{\varepsilon}_t$) simultaneously by casting the incremental constitutive equations in the form of a gradient matrix pre-multiplying the vector of unknowns to give the 'forcing' functions. Because of the multitude of variables even in a plane stress problem, a simple iterative approach which exploits the dependence of $\underline{S}_R^*$ and B on $\underline{\varepsilon}_t$ is adopted here instead. This involves the use of Eqs. (4) and (8) to eliminate $\underline{S}_R^*$ and B from Eq. (31). In particular, use of Eq. (4) allows Eq. (32) to be rewritten as:

$$\underline{S}_{d,\alpha}^* = (1-\alpha)[\underline{S}_i^* - 2/3 \ AE(\underline{\varepsilon}_{t,i})] + \alpha[\underline{S}_{i+1}^* - 2/3 \ AE(\underline{\varepsilon}_{t,i} + \Delta\underline{\varepsilon}_t)] \tag{34}$$

Noting the scalar relationship $\dot{\varepsilon}_{t,eq} = (\sigma_{d,eq}/BV)^N$, integration of Eq. (8) yields the relationship between the non-dimensional drag-stress and the incremental transient strain. The α-form of this relationship is:

$$B_\alpha = [B_o^2 + 2 \ \dot{\varepsilon}_o^{1/3} \ \tilde{H}E/V \int \dot{\varepsilon}_{t,eq}^{1/3} \ dt]_\alpha^{1/2} \tag{35}$$

where $\dot{\varepsilon}_{t,eq}$ is approximated as:

$$\dot{\varepsilon}_{t,eq}^2 = 2/3 \ (\Delta\underline{\varepsilon}_t/\Delta t)^T \underline{H} \ (\Delta\underline{\varepsilon}_t/\Delta t) \tag{36}$$

With $\underline{S}_R^*$ and B eliminated from Eqs. (32) ad (33), $\Delta\underline{\varepsilon}_t$ in Eq. (31), like $\Delta\underline{\varepsilon}_v$ in Eq. (28), can be expressed as a function of the deviatoric stress at time $t=t_{i+1}$, i.e., $\underline{S}_{i+1}^*$. The analytical expression can be written as:

$$\Delta\underline{\varepsilon}_t = \frac{\dot{\varepsilon}_o \lambda_{d,\alpha} \Delta t \{(1-\alpha)[\underline{S}_i^* - 2/3\ AE\underline{\varepsilon}_{t,i}] + \alpha[\underline{S}_{i+1}^* - 2/3\ AE\ \underline{\varepsilon}_{t,i}]\}}{1 + 2/3\ \alpha AE\ \dot{\varepsilon}_o \lambda_{d,\alpha} \Delta t} \tag{37}$$

Since $\lambda_{d,\alpha}$ is dependent on $\Delta\underline{\varepsilon}_t$, Eq. (37) is in fact an implicit relation for $\Delta\underline{\varepsilon}_t$. For the given $\underline{S}_{i+1}^*$ at iteration k, Eq. (37) is iterated to obtain $\Delta\underline{\varepsilon}_t$. This is added to $\Delta\underline{\varepsilon}_v$ to give $\Delta\underline{\varepsilon}_{cr}$, which in turn is used to estimate $\underline{\sigma}_{i+1}$ and hence $\underline{S}_{i+1}^*$ at iteration k+1.

In the following numerical simulations α is set to 1, i.e., the backward (implicit) Euler method is used. Typically, more than fifteen iterations are needed for convergence at the lower level for the highly stressed elements. This is unattractive since iterations are needed at each integration point within an elemet (four in the case of a quadrilateral element), and highly stressed elements may occur often in a typical finite element grid consisting of more than 130 elements.

A lower-level algorithm that combines a Newton-Raphson or tangent type iteration with the α-method is developed to accelerate convergence. This can be derived from Eq.(21), which can be rewritten as:

$$\underline{f}(\Delta\underline{\sigma}) = \Delta\underline{\sigma} - \underline{D}(\Delta\underline{\varepsilon} - \Delta\underline{\varepsilon}_{cr}) \tag{38}$$

where $\Delta\underline{\varepsilon}$ is prescribed and $\Delta\underline{\varepsilon}_{cr}$ can be determined from expressions of the form stated in Eqs. (28) and (37). Expanding $\underline{f}(\Delta\underline{\sigma})$ in a Taylor series, the following expression is obtained:

$$[\Delta\underline{\sigma} - \underline{D}(\Delta\underline{\varepsilon} - \Delta\underline{\varepsilon}_{cr})]^k + \left[\frac{\partial \underline{f}}{\partial \Delta\underline{\sigma}}\right]^k (\Delta\underline{\sigma}^{k+1} - \Delta\underline{\sigma}^k) = \underline{0} \tag{39}$$

Note the following expressions:

$$\Delta\underline{\sigma}^k = \underline{\sigma}_{i+1}^{\ k} - \underline{\sigma}_i \tag{40a}$$

$$\Delta\underline{\sigma}^{k+1} = \underline{\sigma}_{i+1}^{\ k+1} - \underline{\sigma}_i \tag{40b}$$

$$\Delta\underline{\sigma}^{k+1} - \Delta\underline{\sigma}^k = \underline{\sigma}_{i+1}^{\ k+1} - \underline{\sigma}_{i+1}^{\ k} \tag{40c}$$

It is then easily verified that

$$d\underline{\Delta\sigma} = d\underline{\sigma}_{i+1} \tag{41a}$$

Also, since $\underline{\sigma}_\alpha = (1-\alpha)\underline{\sigma}_i + \alpha\,\underline{\sigma}_{i+1}$, it follows that

$$d\underline{\sigma}_\alpha = \alpha\, d\underline{\sigma}_{i+1} \tag{41b}$$

Eqs. (41a, b) will be of use in the following derivation. The derivative in Eq. (39) is easily derived from Eq. (38) as:

$$\left[\frac{\partial f}{\partial \underline{\Delta\sigma}}\right]^k = \left[\underline{I} + \underline{D}\frac{\partial \underline{\Delta\varepsilon}_{cr}}{\partial \underline{\sigma}_{i+1}}\right]^k \tag{42}$$

where

$$\frac{\partial \underline{\Delta\varepsilon}_{cr}}{\partial \underline{\sigma}_{i+1}} = \alpha\,\frac{\partial \underline{\Delta\varepsilon}_{cr}}{\partial \underline{\sigma}_\alpha} \tag{43}$$

It is necessary to evaluate the derivatives of the creep strain components separately. For the steady-state component, differentiation of Eq. (6) followed by substitution of Eqs. (9a) and (9c) yields:

$$\frac{\partial \underline{\Delta\varepsilon}_v}{\partial \underline{\sigma}_{i+1}} = \alpha\,\Delta t\left[\lambda\underline{G} + \frac{3}{2}\,\sigma_{eq}^{-1}\,\frac{\partial\lambda}{\partial\sigma_{eq}}\,\underline{S}^*\,\underline{S}^{*T}\right]_\alpha^k \tag{44}$$

Since the incremental transient strain depends on $\underline{\sigma}_{i+1}$ through $\underline{\sigma}_{d,i+1}$ and BV, the corresponding derivative, i.e., $\partial\underline{\Delta\varepsilon}_t/\partial\underline{\sigma}_{i+1}$, is obtained via the chain rule and is equal to $\partial\underline{\Delta\varepsilon}_t/\partial\underline{\sigma}_{r,i+1}$. Hence, the required derivative can be evaluated using Eq. (44) by replacing $\underline{\sigma}$ with $\underline{\sigma}_d$. Note that this automatically implies replacing σ_{eq} by $\sigma_{d,eq}$, λ by λ_d, and $\underline{S}^*$ by $\underline{S}_d{}^*$.

The required equation for the iterative process is obtained by substituting Eq. (43) in Eq. (42), and finally in Eq. (39). Denoting the elastic compliance matrix by $\underline{C}$, the final result can be written as:

$$\underline{\sigma}_{i+1}{}^{k+1} - \underline{\sigma}_{i+1}{}^{k} = \underline{D}'\,[\underline{C}(\underline{\sigma}_i - \underline{\sigma}_{i+1}{}^{k}) + (\underline{\Delta\varepsilon} - \underline{\Delta\varepsilon}_{cr}{}^{k})] \tag{45}$$

where $\underline{D}'$ is easily identified as the elastic-creep stiffness matrix:

$$\underline{D}' = \left[\underline{C} + \frac{\partial \Delta \underline{\varepsilon}_{cr}^{\,k}}{\partial \underline{\sigma}_{i+1}}\right]^{-1} \tag{46}$$

The matrix $\underline{D}'$ (global form) is used as the tangent stiffness in the BFGS algorithm. Iteration on Eq. (45) yields the stress at i+1. Convergence is defined to occur when the maximum absolute value of the relative change in point stresses between iterations k and k+1 ≤ 0.001. Application of this iterative scheme with α=1 shows that convergence is typically achieved in five to ten iterations.

Code Verification.-- The finite element analysis algorithm has been implemented in a computer code called DECNEC. The current implementation is a two-dimensional version for plane stress problems and uses a four-noded quadrilateral element. The accuracy of the computer code and the algorithm described above has been verified in several simple test cases. They include (1) a rectangular element subjected to a constant displacement-rate normal to one of its edges and with normal movement constrained on the other three sides, and (2) the same constrained element subjected to uniform compressive stress normal to one of its sides (see Fig. 1). These simulate uniaxial loading under constant displacement-rate and constant stress, respectively. The results compare well with those obtained from solving the simultaneous differential equations governing ice deformation (Eqs. (1) - (9)) using the DVERK routine (Runge-Kutta-Verner fifth and sixth order algorithm) in the IMSL package. These results are shown in Figs. 2 and 3. The experimental data in Fig. 2 refer to the uniaxial constant displacement-rate tests on columnar-grained sea ice by Wang [26], while those in Fig.3 refer to creep tests on granular snow-ice by Brill and Camp (reported in Sinha [27]).

NUMERICAL SIMULATIONS

Description of Case Studies.-- Numerical simulations are performed for the nine cases listed in Table 2. Two simulations are run for each case: the first uses the pure flow model and the second uses the combined flow and crack model. Additional simulations are carried out using a version of the combined model which does not take into account transient or anelastic deformation.

The first case serves as a reference for the other eight cases. It corresponds to an ice sheet moving at the velocity of 3 ft/hr (0.91 m/hr) against

a vertical cylindrical indenter of diameter 350 ft (106.68 m) at the ambient temperature of -10°C. The time increment used for analysis in the reference case is 50 seconds and the mesh is of type A (to be explained). The base velocity of 3 ft/hr, about four times greater than that used in an earlier study (Chehayeb et al. [8]), is used to simulate a faster rate of loading. This allows the study of the effect of cracking on the indentation process. The rate of loading, however, is slow enough to limit the amount of cracking to a level that can be handled numerically without encountering instability and incurring great costs.

The eight cases explore the influence of various parameters on the ice pressure generated during indentation. Cases 2 and 3 demonstrate the influence of ice sheet velocity. Case 4 attempts to quantify the effect of a smaller indenter, while Case 5 shows the effect of a grounded rubble pile or an accreted ice foot. Since the material model is rate sensitive, it is important that the effect of different time increments, if any, should be studied, and this is the objective of Cases 6 and 7. Cases 8 and 9 seek to investigate if the results are mesh dependent. All cases are run for fifty minutes.

Numerical Implementation.-- A typical finite element mesh used in this study is illustrated in Fig. 4. The analysis is based on the upstream portion of the ice sheet (a quarter-plane) because the portion on the downstream has hardly any contact with the indenter (Ponter et al. [3]). The criteria for setting up the mesh have been described in Chehayeb et al. [8]. Three mesh types, A, B, and C are used in the simulations (see Table 2). Mesh A has nine circumferential and fourteen radial elements (Fig. 4), Mesh B has twelve circumferential and eighteen radial elements, and Mesh C has six circumferential and ten radial elements. The simulations for all nine cases are carried out with the assumption of a roller interface condition between the ice sheet and the indenter. This condition represents a free interface with no frictional stresses.

For a given time step, the excitation is defined in terms of an imposed displacement in the z-direction at the far-field boundary nodes. This displacement value is made to increase linearly in time, consistent with the chosen uniform velocity.

The choice of time increment is of considerable importance when the constitutive model is described by stiff differential equations. This is often the case for a model formulated with internal variables (Shih [28]). This particular study has found that a time increment of 50 seconds is a reasonable compromise between accuracy and computational effort.

Discussion of Results.-- Table 3 summarizes all the results for the nine test cases. The maximum interface pressure is determined as the maximum stress developed at the interface during the simulation period of fifty minutes. The global force during indentation is calculated from the stresses in the innermost layer of elements. The global pressure is defined as the global force divided by the indenter diameter and the ice sheet thickness. Since there are four integration points in each element, a weighting procedure is used as in Cook [29] to adequately account for the contribution from each point.

The results for the global pressure obtained from the flow and combined models are compared first. Table 3 shows that the global pressures obtained from both models are approximately the same in all cases, except in Case 3 where the global stress versus time relationship predicted by the combined model displays a pronounced softening behaviour with a 'residual' pressure about 60% of the peak value (see Fig. 5). It should be noted that in the majority of the cases the global pressure predicted by the combined model is apparently slightly greater than that predicted by the pure flow model. This, however, is caused by the cracking which perturbs the global pressure and causes it to fluctuate slightly about the value predicted by the flow model. Moreover, the insensitivity of the global pressure to cracking, except for Case 3, is the consequence of the facts that no cracks are assumed to exist in the ice sheet before indentation and that creep flow rather than cracking governs the ice response. Even in Case 3 the cracking does not occur rapidly enough and in sufficiently great quantities to yield a maximum global stress prediction different from that of the flow model, although subsequent cracking does reduce the global pressure significantly. In fact, the average strain-rate determined from the ratio of the velocity to twice the indenter diameter is only 2.4×10^{-6} s^{-1} in Case 3. The situation just described has its counterpart in high rate tests. Timco [1] has observed that there is no apparent difference between indentation and penetration loads at high rate tests (10^{-2} s^{-1} to 10 s^{-1}). He attributed this to the almost instantaneous formation of cracks when the test specimen comes into contact with the indenter. The indenter is in fact interacting with damaged ice on impact and, as a result, the indentation and penetration loads are not much different. Timco has also remarked that a difference between the two loads is indeed observed at lower rate tests. This agrees with the results of this study since the residual global pressure in Case 3 can be interpreted as the penetration pressure, as opposed to the peak global pressure which corresponds to the indentation pressure.

Table 3 shows that the maximum interface normal pressures predicted by the flow model are greater than those predicted by the combined model, except for case 3. These results suggest that when the amount of cracking is small as in low rate tests, the local stresses at the ice-structure interface tend to be relieved. As the loading rate increases, cracking may occur fast enough to cause complete failure of the some of the interface elements and the reduction in contact area tends to increase the interface pressure. An examination of the crack pattern for Case 3 shows that three interface elements have completely failed during the simulation period, and this loss of contact area may account for the higher local pressure predicted by the combined model compared to that predicted by the flow model.

Since the ice-structure interaction process can only be realistically simulated by taking into account the effect of cracking, only the results predicted by the combined model are interpreted in the remaining part of this discussion. Table 3 shows that in all cases except Case 3 the maximum interface pressure is less than 10% higher than the global pressure. For Case 3, the maximum interface pressure is about 50% and 25% greater than the residual and peak global pressures, respectively. This suggests that the moderate amount of cracking has a greater effect on the local interface pressure than the global pressure.

Comparison of Case 2 with the reference case shows that reducing the ice sheet velocity by one-third leads to a 14% reduction in the global and the interface pressures. This is in good agreement with the predictions of an approximate theoretical model, valid for flow with negligible cracking, which suggests that the pressure varies with the $(1/N)^{th}$ power of velocity (Chehayeb et al. [8]). On the other hand, comparison of Case 3 with the reference case suggests that the flow model is no longer valid when cracking is not neligible.

Results for Cases 4 and 5 show that a 30% decrease of indenter size relative to the reference case increases the global and interface pressures by about 14%, while a relative increase of indenter size by 40% decreases the pressures by about 12%. The smaller indenter experiences larger global pressure, although the global force is larger for the larger indenter. These results agree with those in the earlier study by Chehayeb et al. [8], since the small amount of cracking in these cases does not have a significant effect on the ice response.

The effect of time increment on the global and interface pressures can be seen by comparing their values for Cases 1, 6 and 7 in Table 3. The global pressure may not be affected, but differences do exist between the interface

pressures. Furthermore, if the history of the global pressure is examined for the three cases, it is found that although the difference appears to be neligible at steady state, some discrepancies are observed at small times (or strains) when transient creep dominates. The error largely arises because of the difficulties associated with integrating the stiff and highly coupled constitutive equations of the transient creep model.

The results for Cases 1, 8 and 9 show that the global pressure is essentially independent of mesh type (see Fig. 6). Some discrepancy can be seen in the interface pressures, but overall it can be concluded that the results are only slightly mesh-dependent. It should however be noted that mesh sensitivity occurs for the descending branch of the curve in Fig. 5, although the peak and residual global pressures are not influenced by different mesh sizes. Note also that the meshes A, B and C are generated automatically, and the sizes of the ice sheet in the three cases can only be made approximately equal. This has negligible effect on the results, and can be easily confirmed by comparing the predictions of the pure flow model using the three meshes.

The pattern of crack propagation through the ice sheet, useful for studying the ice failure mode, is illustrated for Cases 1 and 3 in Figs. 7 and 8, respectively. In both cases, cracking occurs first in the element which lies along the z-axis and is closest to the indenter. Initially, the orientation of the individual cracked zones tends to be in the radial direction, suggesting that they are formed under hoop stresses. As loading continues, the pattern of propagation is primarily in the radial direction. In Case 1, the amount of cracking is insignificant; none of the elements have completely failed during the simulation period. In Case 3, individual cracked zones can be observed to lie in the circumferential direction in addition to those lying along the radial direction, suggesting that radial stresses are now sufficiently large to cause cracking. Of the nine elements in contact with the indenter, three have completely failed. Elements that are completely cracked can also be found in the second and third layer of elements. These observations show that for low rates of loading radial cracking is present but does not govern ice defomation, while at higher rates of loading, failure may occur by both radial and circumferential cracking which can influence the ice-structure response significantly.

Figure 9 compares the global pressure-time relationships predicted by the combined model and a version of the same model which neglects transient deformation. The simulations are carried out under the conditions of Case 2. It

can be seen that without transient defomation the material fractures prematurely. This is because transient deformation allows the material to store energy while stress redistribution takes place. This reduces the rate of load increase and delays the occurrence of crack formation. In a large ice sheet, considerable amount of energy is absorbed by transient deformation, and the material flows in a ductile manner.

CONCLUSIONS

This paper has presented a finite element method for the analysis of cracking behaviour during ice indentation at low to moderate rates of loading. The numerical simulations are carried out under the assumptions of (i) plane stress conditions, (ii) a roller type of contact between ice and indenter, (iii) an infinite ice sheet with no pre-existing cracks, and (iv) a constant temperature of -10°C. For realistic simulations a flow model which accounts for transient creep is used in conjunction with the smeared cracking model. The solution of the initial boundary-value problem involves the use of a two-level iterative algorithm which employs (i) the BFGS technique to solve the discretized finite element equations, and (ii) a Newton-Raphson technique, combined with the α-method of time integration, to solve the constitutive equations.

Under the loading conditions and assumptions considered in this paper, the simulations indicate that:

(i) Cracking has insignificant effect on the global indentation pressure, although in the case of the moderate rate of loading (Case 3) the global pressure can exhibit softening behaviour resulting in a residual or penetration pressure about 60% of the peak value.

(ii) The maximum local interface pressure is less than 10% greater than the global pressure for the slow rate tests. In Case 3, the local pressure is 25% and 50% greater than the peak and residual global pressures, respectively.

(iii) At low rates of loading (e.g., $< 10^{-6}$ s^{-1}) radial cracking appears but does not affect the ice response significantly. Under more brittle conditions radial cracking, followed by circumferential cracking, relieves the global pressure, but also increases the local pressure due to the loss of contact area.

(iv) Transient creep can influence the ice response. This can occur by delaying the cracking and hence the failure of the ice sheet, or by absorbing a significant portion of the energy of excitation and hence causing ice to flow without much softening.

ACKNOWLEDGEMENTS

The authors would like to acknowledge financial support from BP America, ARCO, AMOCO, CONOCO and MOBIL through MIT's Center for Scientific Excellence in Offshore Engineeing; the U.S. Department of the Interior, Minerals Management Service; and the U.S. Army Research Office through MIT's Center for Advanced Construction Technology.

REFERENCES

1 Timco, G.W., "Indentation and Penetration of Edge-Loaded Freshwater Ice Sheets in the Brittle Range," Proceedings of the Fifth International Offshore Mechanics and Arctic Engineering Symposium, Vol. IV, Tokyo, Japan, 1986, pp. 444-452.

2 Michel, S. and Toussaint, N., "Mechanisms and Theory of Indentation of Ice Plates," Journal of Glaciology, Vol. 19, No. 81, 1977, pp. 285-300.

3 Croasdale, K.R., Morgenstern, M.R. and Nuttall, J.B., "Indentation Tests to Investigate Ice Pressures on Vertical Piers," Journal of Glaciology, Vol. 19, No. 81, 1977, pp. 310-312.

4 Ponter, A.R.S. et al., "The Forces Exerted by a Moving Ice Sheet on an Offshore Structure: Part I The Creep Mode," Cold Regions Science and Technology, Vol. 8, 1983, pp. 109-118.

5 Bruen, F.J. and Vivatrat, V., "Ice Force Prediction Based on Strain-Rate Field," Third International Symposium on Offshore Mechanics and Arctic Engineering, New Orleans, LA, 1984, 7 pp.

6 Ting, S-K. and Shyam Sunder, S., "Sea Ice Indentation Accounting for Strain-Rate Variation," Proceedings of the ASCE Specialty Conference: Arctic '85—Civil Engineering in the Arctic Offshore, San Francisco, California, March, 1985, 11 pp.

7 Shyam Sunder, S., Ganguly, J., and Ting, S-K., "Anisotropic Sea Ice Indentation in the Creeping Mode," Journal of Offshore Mechanics and Arctic Engineering, ASME, Vol. 109, No. 2, 1987, pp. 211-219.

8 Chehayeb, F.S., Ting, S-K., Shyam Sunder, S., and Connor, J.J., "Sea-Ice Indentation in Creeping Mode," Journal of Engineering Mechanics, ASCE, Vol. 113, No. 7, 1987, pp. 965-983.

9 Tomin, M.J., Cheung, M., Jordaan, I.J. and Cormeau, A., "Analysis of Failure Modes and Damage Processes of Freshwater Ice in Indentation Tests," Proc. of the Fifth International Offshore Mechaics and Arctic Engineering Symposium, Vol. IV, 1986, pp. 453-460.

10 Palmer, A.C., et al., "Fracture and Its Role in Determining Ice Forces on Offshore Structures," Annals of Glaciology, Vol. 4, 1983, pp. 216-221.

11 Cormeau, A., et al., "Ice-Structure Interaction: A Fundamental Energy-Based Approach,," IAHR Ice Symposium, Hamburg, 1984, pp. 161-174.

12 Sinha, N.K., Timco, G.W., and Frederking, R., "Recent Advances in Ice Mechanics in Canada," Advances in Ice Mechanics – 1987, ASME, Offshore Mechanics and Arctic Engineering Symposium Committee, Houston, Texas, 1987, pp. 15-35.

13 Cox, G.N.F., et al, "The Mechanical Properties of Multi-Year Sea Ice, Phase II: Test Results," Draft Report, U.S. Army Cold Regions Research and Engineering Laboratory, Hanover, 1984.

14 Frederking, R.M.W. and Timco, G.W., "Compressive Behaviour of Beaufort Sea Ice under Vertical and Horizontal Loading," Proceedings of the Third OMAE Symposium, Vol. III, 1984, pp. 145-149.

15 Sinha, N.K., "Young Arctic Frazil Sea Ice: Field and Laboratory Strength Tests," Journal of Materials Science, Vol. 21, No. 5, 1986, pp. 1533-1546.

16 Sinha, N.K., "Constant Strain- and Stress-Rate Compressive Strength of Columnar-Grained Ice," Journal of Materials Science, Vol. 17, No. 3, 1982, pp. 785-802.

17 Jones, S.J., "The Confined Compressive Strength of Polycrystalline Ice," Journal of Glaciology, Vol. 28, 1982, pp. 171-177.

18 Shyam Sunder, S. and Wu, M.S., "A Differential Flow Model for Polycrystalline Ice," Cold Regions Science and Technology, In Press.

19 Shyam Sunder, S. and Wu, M.S., "A Multiaxial Differential Model of Flow in Orthotropic Polycrystalline Ice," Submitted for Publication.

20 Rashid, Y.R., "Analysis of Prestressed Concrete Pressure Vessels," Nuclear Engineering and Design, Vol. 7, No. 4, 1968, pp. 334-355.

21 Bazant, Z.P. and Cedolin, L., "Blunt Crack Band Propagation in Finite Element Analysis," Journal of the Engineering Mechanics Division, ASCE, Vol. 105, No. EM2, Proc. Paper 14529, April 1979, pp. 279-315.

22 Ting, S.-K. and Shyam Sunder, S., "Constitutive Modeling of Sea Ice with Applications to Indentation Problems," CSEOE Research Report No. 3, Department of Civil Engineering, Massachusetts Institute of Technology. 1985, 255 pp.

23 Cordts, D. and Kollman, F.G., "An Implicit Time Integration Scheme for Inelastic Constitutive Relations with Internal State Variables," International Journal for Numerical Methods in Engineering, Vol. 23, 1986, pp. 533-554.

24 Matthies, H. and Strang, G., "The Solution of Nonlinear Finite Element Equations," International Journal for Numerical Methods in Engineering, Vol. 14, 1979, pp. 1613-1626.

25 Crisfield, M.A., "Accelerating and Damping the Modified Newton-Raphson Method," Computers & Structures, Vol. 18, No. 3, 1984, pp. 395-407.

26 Wang, Y.S., "A Rate-Dependent Stress-Strain Relationship for Sea Ice," Proceedings of the First International Symposium on Offshore Mechanics and Arctic Engineering, ASME, New Orleans, Louisiana, March 1982, PP. 243-248.

27 Sinha, N.K., "Grain-Boundary Sliding in Polycrystalline Materials," Philosophical Magazine A, Vol. 40, No. 6, 1979, pp. 825-842.

28 Shih, C.F., DeLorenzi, H.G., and Miller, A.K., "A Stable Computational

Scheme for Stiff Time-Dependent Constitutive Equations," In Proceedings of Structural Mechanics in Reactor Technology, Paper L2/2, San Francisco, 1977.

29 Cook, R.D., Concepts and Applications of Finite Element Analysis, John-Wiley & Sons, 1981.

NOMENCLATURE

A = parameter describing anelastic deformation

B = non-dimensional drag stress;

B_o = initial drag stress;

$\underline{B}$ = strain rate-nodal velocity matrix;

$\underline{C}$ = elastic compliance matrix;

$\underline{d}$ = true incremental displacement vector;

$\underline{d}'$ = incremental displacement vector

$\underline{D}$ = elastic rigidity matrix;

$\underline{D}'$ = elastic-creep stiffness matrix;

E = Young's modulus;

f = failure criterion

$\underline{f}$ = function of incremental stress;

$\underline{F}$ = internal force vector;

$\underline{G}$ = stress transformation matrix;

$\tilde{H}$ = constant in evolution equation for the drag stress;

$\underline{H}$ = strain-rate transformation matrix;

$\underline{I}$ = identity matrix;

I_1 = first invariant of stresses;

J_2 = second invariant of deviatoric stresses;

k = variable in failure criterion;

$\underline{K}$ = incremental tangent stiffness matrix;

N = power law exponent;

p = variable in failure criterion;

$\underline{P}$ = external force vector;

Q = activation energy for creep;

$\underline{r}$ = incremental nodal residual force vector;

R = universal gas constant;

$\underline{R}$ = back stress vector, or residual force vector;

$\underline{S}^*$ = deviatoric stress vector;

$\underline{S}_{d_*}^*$ = deviatoric stress-difference vector;

$\underline{S}_R^*$ = deviatoric back stress vector;

t = time;

T = temperature;

$\underline{U}$ = nodal displacement vector;

V = stress-factor for compressive loading;

V_o = temperature-independent stress-factor;

W = stress-factor for tensile loading;

$\underline{v}, \underline{w}$ = vectors for use in the BFGS method;

α = parameter in time integrator;

$\dot{\varepsilon}_o$ = reference strain-rate of unity

$\dot{\varepsilon}_{t,eq}$ = equivalent transient strain-rate;

$\dot{\varepsilon}_{v,eq}$ = equivalent steady-state strain-rate;

$\underline{\varepsilon}$ = total strain vector;

$\underline{\varepsilon}_{cr}$ = creep strain vector;

$\underline{\varepsilon}_e$ = elastic strain vector;

$\underline{\varepsilon}_t$ = transient strain vector;

$\underline{\varepsilon}_v$ = steady-state strain vector;

η = parameter found from line search procedure;

λ = associative steady-state flow rule variable;

λ_d = associative transient-flow rule variable;

σ_{cm} = maximum compressive strength;

σ_{cn} = compressive strength;

σ_{eq} = equivalent stress;

$\sigma_{d,eq}$ = equivalent stress-difference;

σ_{tm} = maximum tensile strength;

σ_{tn} = tensile strength;

$\sigma_{xx}, \ldots, \sigma_{zz}$ = normal stress components in Cartesian frame;

$\underline{\sigma}$ = stress vector;

$\underline{\sigma}_d$ = stress difference vector;

ζ = tolerance for slack line search

Ω = volume of a finite element;

$\dot{}$ = time rate of variable; and

Δ = incremental form of variable.

Table 1 - MATERIAL PARAMETERS

Flow Model		Crack Model	
Parameter	Value	Parameter	Value
E	9.5 GPa	σ_{cm}	3.0 MPa
υ	0.3	σ_{tm}	1.8 MPa
N	3	W	105 MPa
V	105 MPa		
A	0.0626		
B_o	0.410		
$\tilde{H}$	0.0855		

Q = 67 KJ/mol, R = 8.314 J/mol/K, T = 263 K

Table 2 – SUMMARY OF CASES

Case	Ice Velocity (ft/hr)	Indenter Diameter (ft)	Time Increment (sec)	Mesh Type	Temp. (°C)
1	3	350	50	A	-10
2	2	350	50	A	-10
3	6	350	50	A	-10
4	3	250	50	A	-10
5	3	500	50	A	-10
6	3	350	25	A	-10
7	3	350	75	A	-10
8	3	350	50	B	-10
9	3	350	50	C	-10

Note: 1 ft = 0.3048 m

Table 3 - SUMMARY OF RESULTS

	Global Pressure (MPa)		Maximum Interface Pressure (MPa)	
Case	Flow Model	Combined Model	Flow Model	Combined Model
1	1.310	1.319	1.445	1.432
2	1.136	1.132	1.252	1.232
3	1.670	1.076*	1.849	2.034
4	1.482	1.500	1.630	1.615
5	1.160	1.156	1.274	1.253
6	1.302	1.319	1.437	1.429
7	1.317	1.319	1.459	1.390
8	1.313	1.335	1.463	1.441
9	1.326	1.332	1.401	1.358

* residual stress; peak stress = 1.7 MPa

FIGURE LEGENDS

Figure 1 Test Problem for Verification of Computer Code

Figure 2 Comparison of Finite Element and Runge-Kutta Routine Results with Uniaxial Compression Test Data on Columnar-Grained Sea Ice by Wang (1982)

Figure 3 Comparison of Finite Element and Runge-Kutta Routine Results with Uniaxial Test Data on Granular Snow-Ice (Reported by Sinha, 1979)

Figure 4 Finite Element Grid for Numerical Simulations

Figure 5 Predictions of Global Pressure vs. Time Using (a) Pure Flow Model, and (b) Combined Flow/Crack Model

Figure 6 Comparison of the Predictions of Global Pressure vs. Time for Three Mesh Types

Figure 7 Pattern of Crack Distribution in Case 1

Figure 8 Pattern of Crack Distribution in Case 3

Figure 9 Predictions of Global Pressure from Comnbined Flow/Crack Model (a) With and (b) Without Transient Creep

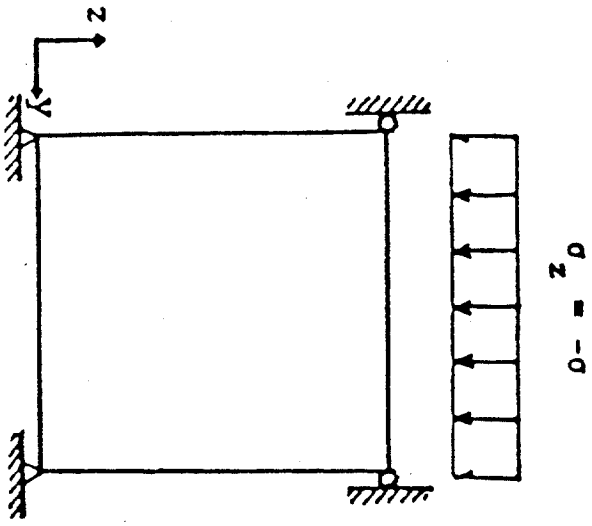
z
y
$\sigma = z_0$

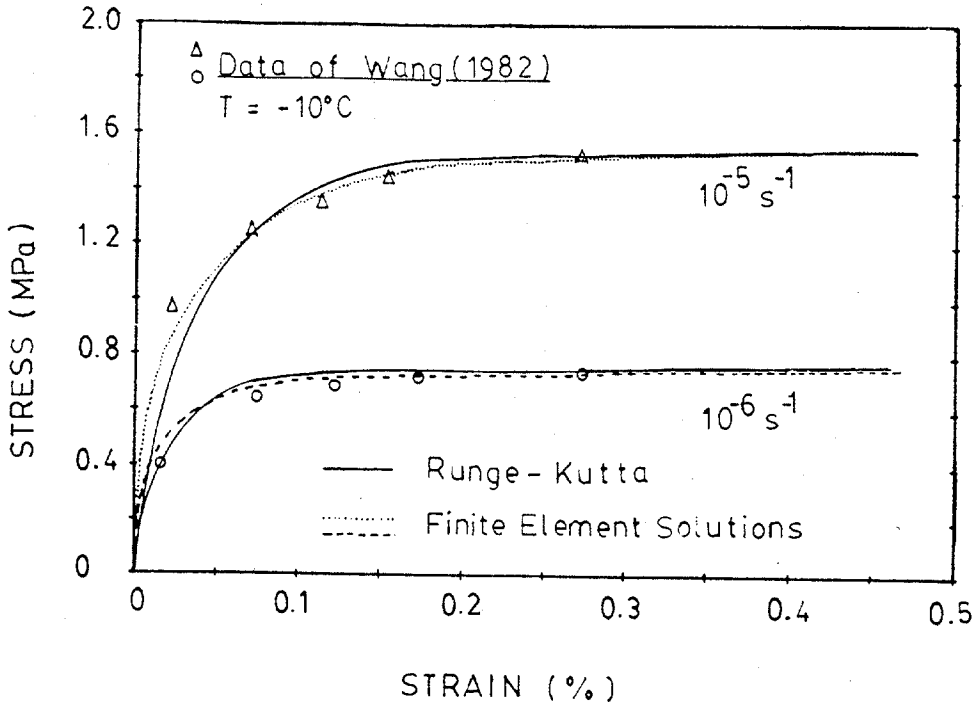
Data of Wang (1982)
T = -10°C
10^{-5} s^{-1}
10^{-6} s^{-1}
Runge-Kutta
Finite Element Solutions
STRESS (MPa)
STRAIN (%)
0
0.4
0.8
1.2
1.6
2.0
0.1
0.2
0.3
0.4
0.5

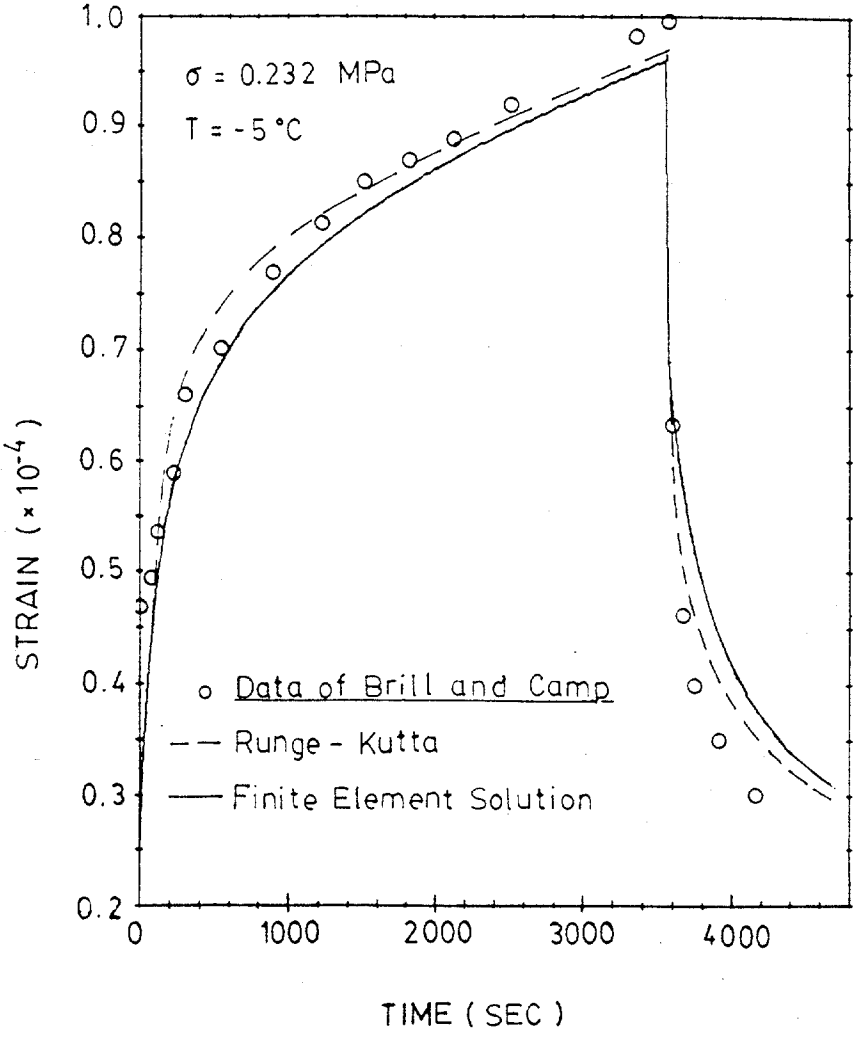
σ = 0.232 MPa
T = -5 °C
o Data of Brill and Camp
Runge - Kutta
Finite Element Solution
STRAIN (× 10⁻⁴)
TIME (SEC)
1.0
0.9
0.8
0.7
0.6
0.5
0.4
0.3
0.2
0
1000
2000
3000
4000

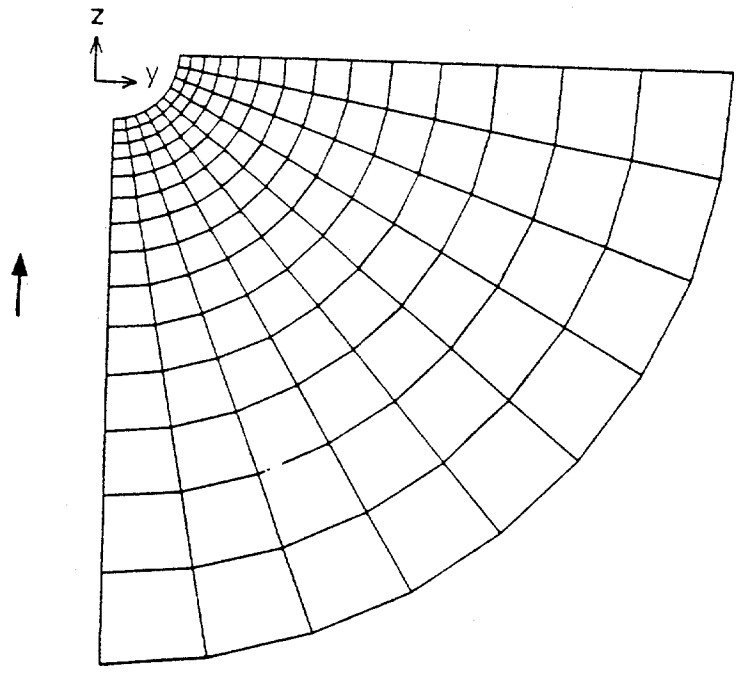
z
y

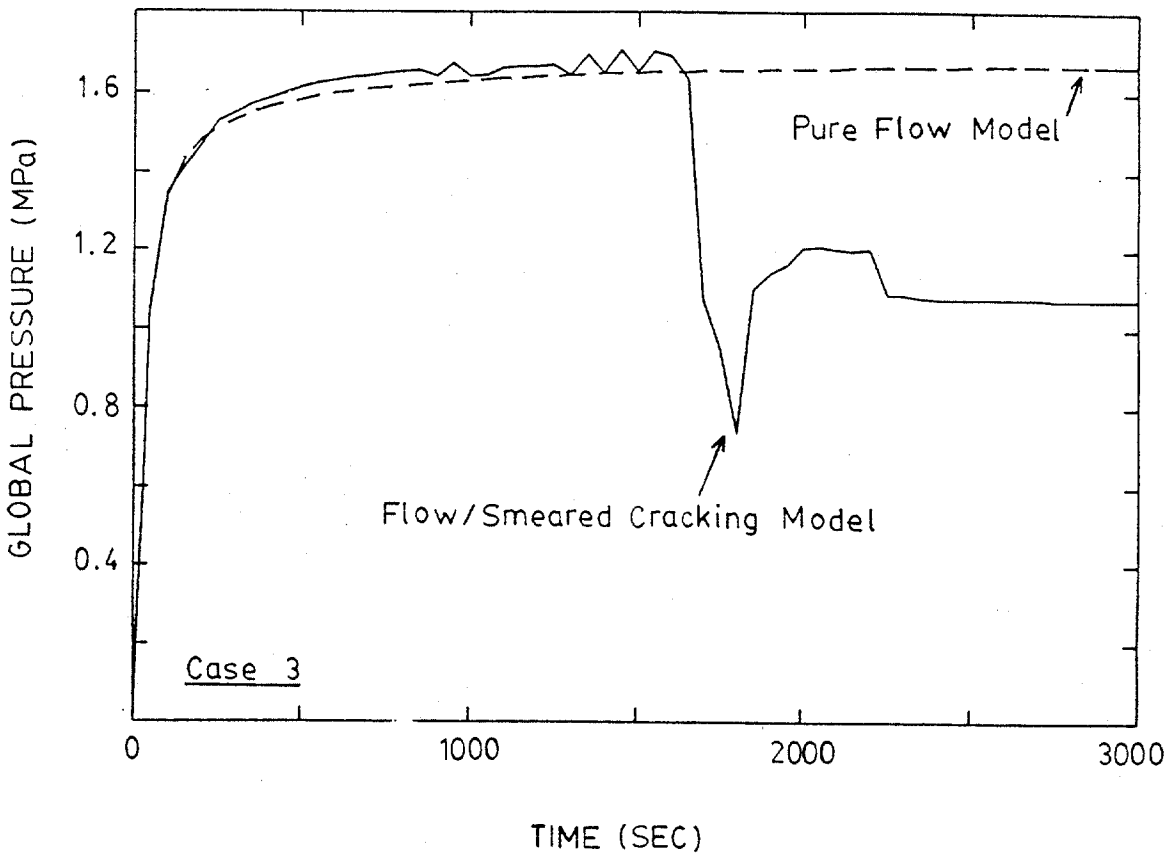
GLOBAL PRESSURE (MPa)
1.6
1.2
0.8
0.4
0
1000
2000
3000
TIME (SEC)
Pure Flow Model
Flow/Smeared Cracking Model
Case 3

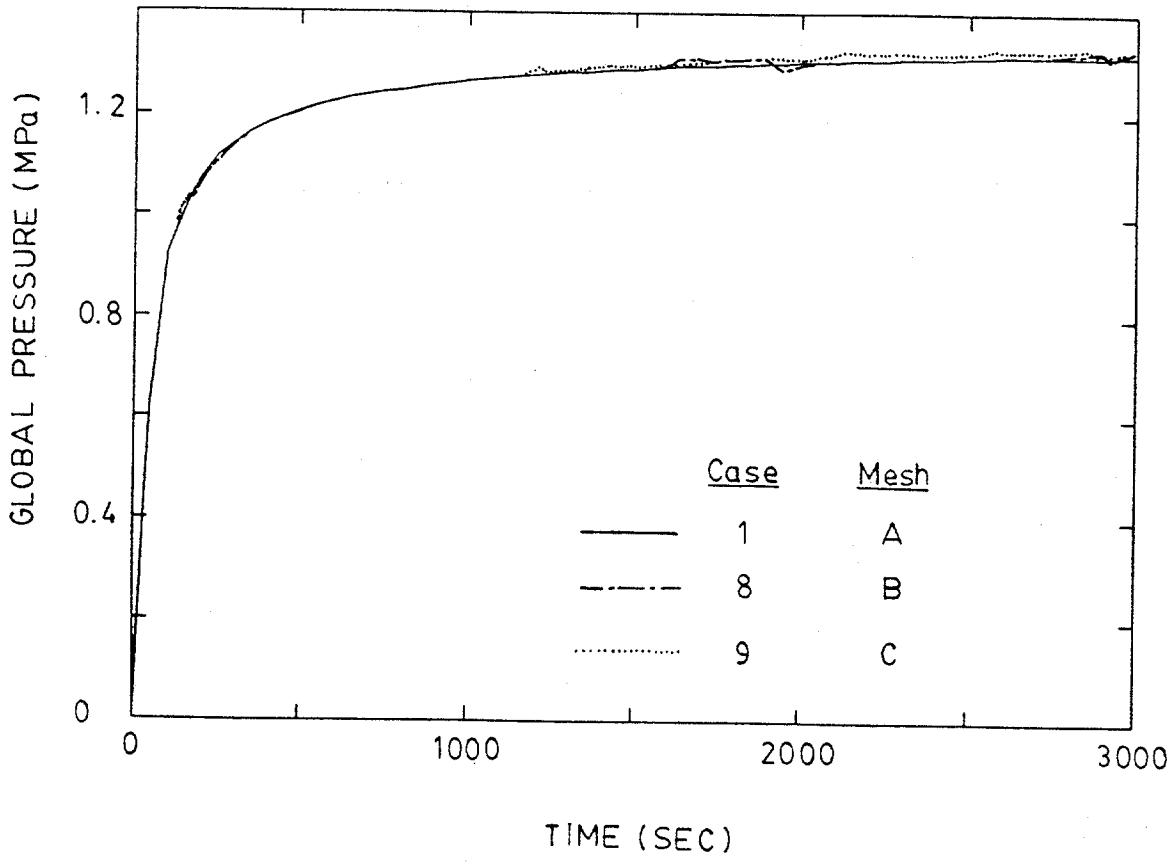
GLOBAL PRESSURE (MPa)
1.2
0.8
0.4
0
0
1000
2000
3000
TIME (SEC)
Case
Mesh
1
A
8
B
9
C

Case 1

/ Crack Orientation At Gaussian Point

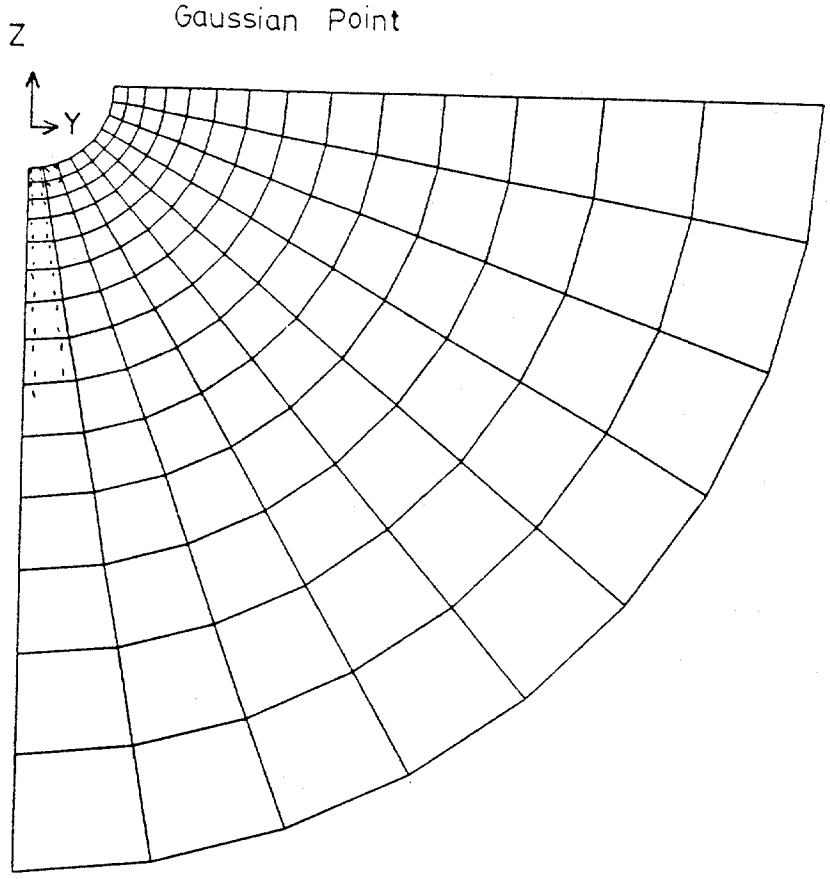

Case 3

\ Crack Orientation At
Gaussian Point

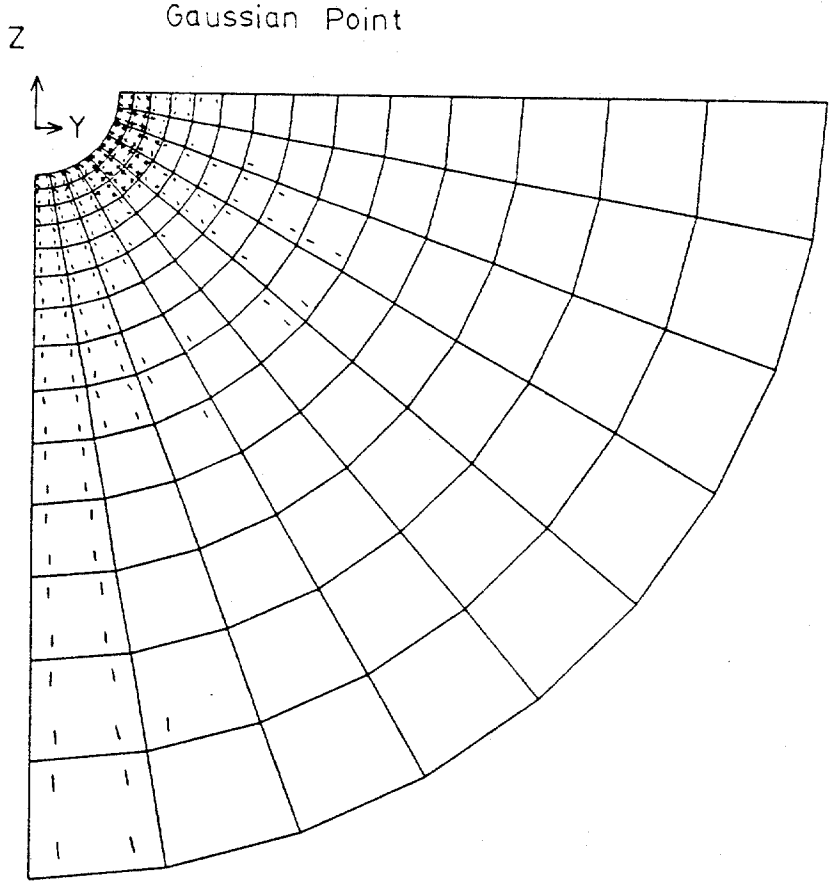

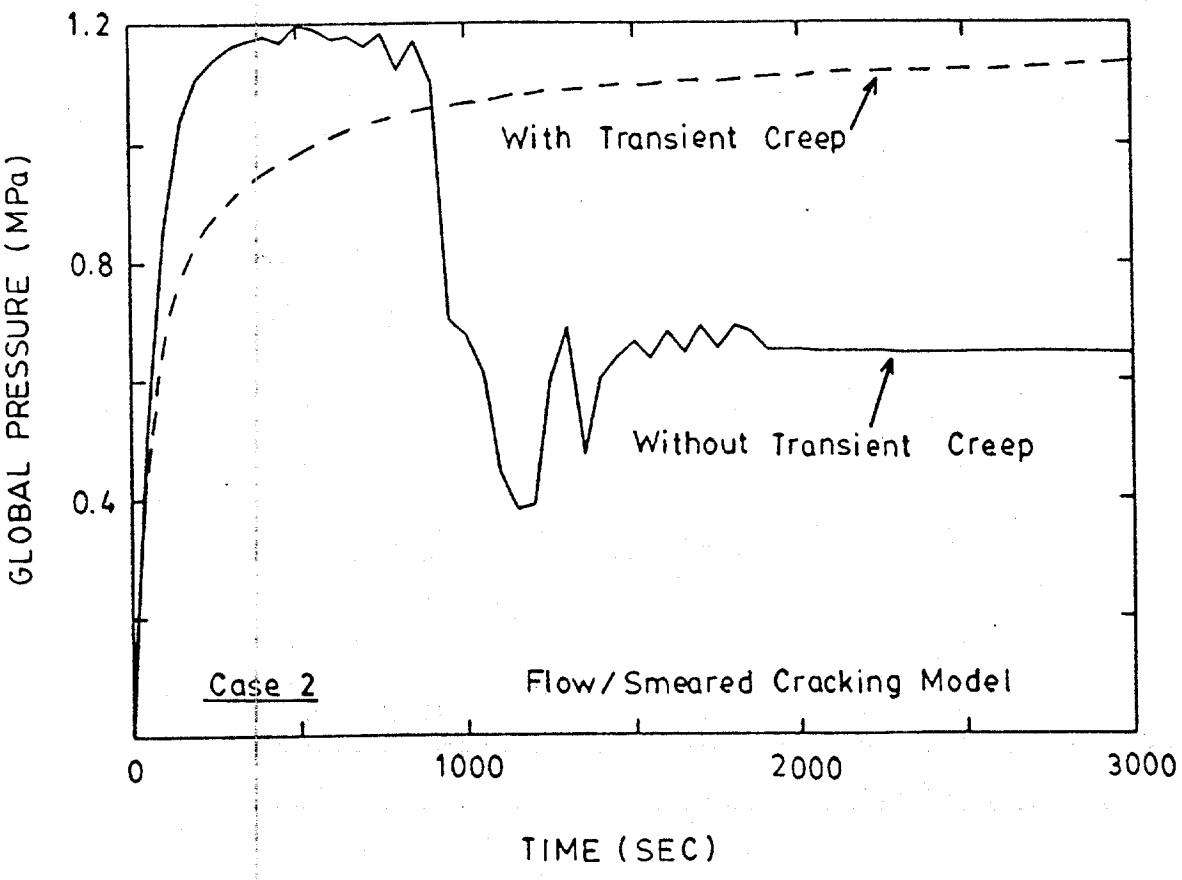
1.2
0.8
0.4
GLOBAL PRESSURE (MPa)
With Transient Creep
Without Transient Creep
Case 2
Flow/Smeared Cracking Model
0
1000
2000
3000
TIME (SEC)